

Gas Transport in the Insensitive High Explosive PBX 9502

Michael A. Englert-Erickson,^{*,[a]} Matthew D. Holmes,^[a] Gary R. Parker,^[a] Chad C. Schmidt,^[b] and Brad A. Meyer^[b]

Abstract: Small-scale laboratory experiments were performed to analyze gas transport mechanics in PBX 9502, an insensitive high explosive (IHE) composition. Two independent investigations are reported here. First, gas permeametry and dynamic pycnometry techniques were used to measure the molecular flow (Knudsen) coefficient and the internally interconnected void fraction of pristine and thermally damaged samples in two uniaxial pressing orientations. The permeability of PBX 9502 was found to be unmeasurably low (of the same order of magnitude as PTFE) with gas transport being diffusion-dominated. Secondly, a pressure vessel experiment was developed to

measure quasi-static and dynamic gas generation as the explosive was heated to self-ignition (cookoff). The gas generation results and the permeability/diffusivity findings provide evidence that PBX 9502 remains impermeable until seconds prior to self-ignition. At ignition, internal void-pressure drives macro-scale cracking and the sample becomes uniformly incorporated in the following deconsolidating deflagration. These results are discussed within the context of previous observations of pressure-dependent cookoff behavior of PBX 9502 and provide a more complete description of thermal damage evolution in this explosive composition.

Keywords: PBX 9502 · Cookoff · Permeability · Diffusivity · TATB

1 Introduction

A thorough understanding of the underlying mechanics and behaviors of non-shock initiation in high explosive compositions is necessary to prevent accidents that may result from inadvertent insult. In the context of explosives safety, an “insult” refers to any event that may transfer energy in sufficient quantity to initiate an exothermic reaction in the energetic material. Since these materials are metastable, their reaction rates are highly temperature-dependent, as described by Arrhenius kinetics [1]. Therefore, if sufficient energy is delivered to the material, a positive feedback loop commences which can culminate in self-ignition (“cookoff”). A fuel-fire is an example of a bulk-heating thermal insult that can lead to cookoff. Moreover, in solid explosives, the elevated thermal environment prior to self-ignition can induce chemical and morphological changes (collectively termed “thermal damage”) that may exacerbate the violence of the final reaction [2].

PBX 9502 (95 wt.% TATB, 5 wt.% Kel-F 800) is classified as an IHE because it can endure significant insults without violent reaction. In reviewing the range of cookoff experiments performed with PBX 9502, no outcome more violent than a containment vessel pressure burst has been reported [3,4]. Previously conducted cookoff experiments have typically focused on collecting high-fidelity, spatially-resolved temperature data with the ultimate goal of predicting the location and time-to-cookoff in specified charge geometries with well-defined boundary conditions [5,6,7]. Holmes, et al. observed the time-to-cookoff for PBX 9502 to be pressure-dependent, with sealed tests cooking off earlier

than vented ones [4]. This indicates that the reaction rate is dependent on the gas generated by the decomposing sample [6]. It is well-known that the reaction rate of a deflagrating explosive is pressure dependent [8]: the increased pressure compresses the location of exothermic gas-phase reactions closer to the surface of the un-consumed solid material, thereby increasing heat transferred to the un-reacted material. Furthermore, TATB’s autocatalytic thermal decomposition [6] serves as a mechanism by which increased pressure serves to elevate the solid-state chemistry of the material, in the absence of flame. The role of gas transport mechanics during the thermal decomposition and cookoff of PBX 9502 remains unclear.

2 Experimental Section

Two independent studies were devised to investigate the gas transport mechanics and measure the dependence of thermal decomposition on gas pressure. The first, a “flow-parameter” experiment measured the diffusivity, in both

[a] M. A. Englert-Erickson, M. D. Holmes, G. R. Parker
Explosive Science and Shock Physics
Los Alamos National Laboratory
Los Alamos, 87544, NM, USA
*e-mail: m.erickson@lanl.gov

[b] C. C. Schmidt, B. A. Meyer
Gas Transfer Systems
Los Alamos National Laboratory
Los Alamos, 87544, NM, USA

Table 1. Physical parameters of the pristine samples used for permeability and dynamic pycnometry experiments.

	Machined	Cleaved
Length (cm)	1.50	1.29
Diameter (cm)	1.00	1.00
Mass (g)	2.210	1.894
Density (g/cm ³)	1.876	1.876
ϵ_{total}	0.033	0.033

Table 2. Physical parameters of thermally damaged samples used for permeability and dynamic pycnometry experiments.

	Axial	Orthogonal
Length (cm)	1.52	1.51
Diameter (cm)	1.01	1.01
Mass (g)	2.202	2.204
Density (g/cm ³)	1.808	1.822
ϵ_{total}	0.069	0.062

pristine (non-damaged) and thermally damaged samples, of this composition under thermally static, ambient temperature conditions. The first measurement technique used in the flow parameter experiment was a gas-style permeameter, in which an initial pressure gradient was established across the two end faces of a cylindrical sample. The change in pressure, across the sample as a function of time was measured to determine the Darcy flow [9] through the material. The sample was sealed on the circumferential face with a PTFE sleeve which was radially compressed. Pristine samples of PBX 9502 were used to test how machining smearing, caused by binder melt, might close off surface pore geometry and limit gas flow through the sample. For this, pristine machined and cleaved samples were used, and physical parameters concerning them can be found in Table 1. Equation (1) represents the relationship between the porosity (ϵ_{total}), theoretical maximum density, and measured parameters for each sample tested.

$$\epsilon_{\text{total}} = 1 - \frac{\rho_{\text{sample}}}{\text{TMD}} \quad (1)$$

Thermally damaged samples were machined in two directions, axially and orthogonally (in relation to the pre-ma-

chined uniaxial pressing), to test how the anisotropic crystalline nature of PBX 9502 and ratchet growth [10] might affect gas flow. Table 2 gives physical parameters for these samples.

A constant upstream pressure (207 kPa) of helium was maintained, with a vacuum (less than 0.13 Pa) held on the downstream side, and the mass flow rate was recorded with a helium mass spectrometer leak detector. Early testing revealed that the permeability of the explosive was of the same order of magnitude as that of the PTFE gasket.

This necessitated the development of a novel measurement technique named dynamic pycnometry. This method consisted of placing a sample of material inside a small pressure vessel, purging the vessel of ambient air, charging the vessel and sample with helium (approximately 690 kPa) for an extended duration to permit complete saturation of the explosive sample, rapidly evacuating (target evacuation time 0.2 s), resealing the vessel, then measuring the pressure rise of helium outgassing from the sample. Dynamic pycnometry was used to determine the gas flow parameters in a thermally static environment.

The second “gas generation” experiment observed the dynamic thermal evolution up to and through self-ignition using samples with varying surface area to volume ratios to infer the relationship between thermal damage and permeability. Samples were placed inside of a small pressure oven and heated at 325 °C to self-ignition. The oven itself was designed to survive and contain the full pressurization of deflagration (internal volume $97.0 \pm 0.1 \text{ cm}^3$). Four sample test series, as shown in Table 3, were prepared via uniaxial pressing (density of $1.90 \pm 0.02 \text{ g/cm}^3$, nominal mass 2.2 g). Gas pressurization rates for all samples were measured and from this data, a gas generation rate was calculated to infer the dynamic thermal evolution of permeability in this composition. Dynamic and quasi-static pressure, sample temperature, time-lapse, and high-speed video data were recorded for all tests.

Table 3. Physical parameters of PBX 9502 samples used in gas-generation experiments.

Test Series	Sample Diameter (mm)	Sample Height ± 0.1 (mm)	Volume (mm ³)	Surface Area (mm ²)	Volume/SA Ratio
A	10	15	1178 ± 8	628 ± 3	1.88 ± 0.02
B	19.05	4.1	1170 ± 30	815 ± 6	1.43 ± 0.05
C ^{a)}	10	5	1180 ± 20	942 ± 9	1.25 ± 0.03
D	25	2.4	1180 ± 50	$1170. \pm 8$	1.01 ± 0.05

a) Test series C consisted of three separate small cylinders of given dimensions. Volume and Surface Area are net values of all three cylinders.

3 Results and Discussion

3.1 Flow Parameter Experiment

3.1.1 Gas Permeameter Method

Equation (2) is the combined transport equation of continuity and momentum in porous media and will be used to calculate the interconnected void fraction ε , with D^k as the diffusion (Knudsen) coefficient, ρ the gas density, α_n the permeability, and μ as gas viscosity [11].

$$\varepsilon \frac{\partial \rho}{\partial t} = \nabla \left(\frac{\alpha_n \rho}{\mu} \nabla P - D^k \nabla \rho \right) \quad (2)$$

The flow rate through an explosive sample with a PTFE gasket was measured to be 29 mPa cm³/s, while flow through an impermeable steel plug with the PTFE gasket was measured to be 11 mPa cm³/s. The advective flow rate through the sample – despite the choice of helium as a transport molecule – was negligibly small. As shown, the observed flow rate was of the same order of magnitude as control experiments using an impermeable steel plug in place of the explosive sample, indicating that the permeability of the explosive is not measurably greater than that of the PTFE sealing gasket. This allows for the omission of advection and pressure-gradient driven processes from the solution.

Therefore, assuming that all gas flow through the explosive is in the molecular regime (purely diffusive), and in the axial direction through a homogenous and isotropic sample, equation (2) is simplified into equation (3), with initial condition (4), boundary conditions (5), and solution (6).

$$\frac{\partial \rho}{\partial t} = \frac{D^k}{\varepsilon} \frac{\partial^2 \rho}{\partial x^2} \quad (3)$$

$$\rho(x, 0) = 0 \quad (4)$$

$$\rho(0, t) = \rho_0 \quad (5a)$$

$$\rho(L, t) = 0 \quad (5b)$$

where L is the sample length, and ρ_0 is the upstream gas density, thus

$$\dot{m} = -D^k A \left. \frac{\partial \rho}{\partial x} \right|_{x=L} \quad (6)$$

$$= \frac{D^k A \rho_0}{L} \left(1 + 2 \sum_{n=1}^{\infty} (-1)^n e^{-\left(\frac{D^k}{L^2}\right) n^2 \pi^2 t} \right)$$

Furthermore, the mass flow rate at steady state can be determined by letting $t \rightarrow \infty$, which simplifies (6) into equation (7).

$$\dot{m}_{ss} = \frac{D^k A \rho_0}{L} \quad (7)$$

Thus using equations (6) and (7) (transient and steady-state mass flow rate, respectively), the measured mass flow rate was used to calculate the interconnected void fraction and molecular flow coefficient (Table 4).

In order to compare the machined sample to the cleaved version (due to the length difference), equation (6) was used to reconstruct the mass flow through the machined sample using the presented values, in Table 4, for D^k and ε . This small correction for the length difference revealed that machining smearing on the surface did not play a significant role as the corrected machined sample flow was of the same order of magnitude as the cleaved sample flow.

In analyzing Table 4, it is observed that the calculated interconnected void fraction is larger than the porosity that was found for both samples (Table 1). This physical impossibility is most likely a consequence of the assumption of solely axial flow. As previously mentioned, testing revealed that the flow rate through the PTFE gasket was of the same order of magnitude as the samples that were tested. In developing equation (3) it was assumed that the gas pathway was purely in the axial direction, and any gas exchange between the gasket and sample was negligible. However, given these results, radial flow between the gasket and sample may account for part of this discrepancy. Additionally, it was assumed that the gasket made a perfect seal with the sample, but bypass flow between the gasket and sample may also contribute to error in this method. In an effort to more accurately characterize the transport phenomena, a second method was developed.

3.1.2 Dynamic Pycnometry Method

In the pycnometry experiment, the cylindrical sample is unconfined in a small vessel, free to outgas on all faces. The helium outgassing from each presumably homogenous and isotropic sample was assumed to be axisymmetric. This allows equation (2) to be simplified into equation (8) in radial

Table 4. Measured values and calculated results for diffusion coefficient and interconnected porosity for each sample.

	Machined	Cleaved
ΔP (kPa)	208.1	206.5
Steady State Leak Rate (mPa cm ³ /s)	21	41
D^k/ε (cm ² /s)	5.9×10^{-6}	7.5×10^{-6}
D^k (cm ² /s)	2.0×10^{-7}	3.3×10^{-7}
ε	0.034	0.045

coordinates, where r is the radial direction and z the axial direction.

$$\varepsilon \frac{\partial \rho}{\partial t} = D^k \left(\frac{\partial^2 \rho}{\partial r^2} + \frac{1}{r} \frac{\partial \rho}{\partial r} + \frac{\partial^2 \rho}{\partial z^2} \right) \quad (8)$$

Like equation (3), equation (8) can be solved exactly, with the initial condition (9) and boundary conditions (10), where r_0 is the radius of the sample, ρ_0 the charged gas density, and ρ_i the evacuated container gas density.

$$\rho(r, z, 0) = \rho_0 \quad (9)$$

$$\rho(r_0, z, t) = \rho_i \quad (10a)$$

$$\rho(r, 0, t) = \rho_i \quad (10b)$$

$$\rho(r, L, t) = \rho_i \quad (10c)$$

The solution of equation (8) can be represented as the product of two partial solutions for the r and z directions, which is given in equation (11).

$$\rho(r, z, t) = R(r, t) \cdot Z(z, t) \quad (11)$$

With each partial solution R and Z given by equations (12) and (13) [12].

$$R(r, t) = 2(\rho_0 - \rho_i) \sum_{m=1}^{\infty} \frac{J_0(\lambda_m r) e^{-\lambda_m^2 r_0^2 \left(\frac{t}{\tau}\right) \left(\frac{1}{r_0}\right)}}{(\lambda_m r_0)^2 J_1} \quad (12)$$

$$Z(z, t) = \frac{4}{\pi} \sum_{n=0}^{\infty} \frac{\sin \left[(2n+1) \left(\frac{\pi z}{L}\right) \right]}{2n+1} e^{-(2n+1)^2 \pi^2 \left(\frac{t}{\tau}\right) \left(\frac{1}{L}\right)} \quad (13)$$

in which J_0 and J_1 are Bessel Functions of the first kind, and $\lambda_m r_0$ are the eigenvalues of J_0 . The mass of gas loss from the sample is then given by equation (14), where V_s is the sample volume.

$$m_t = (\rho_0 V_s - \int \int \int \rho(t) dV) \quad (14)$$

Equation (14) is rewritten using solutions (12) and (13). This is shown as equation (15).

$$m_t = \rho_0 V_s - \int_0^L \int_0^{r_0} 2\pi r R(r, t) Z(z, t) dr dz \quad (15)$$

Equation (15) can be rearranged into equation (16), which allows for the explicit solving of the involved integrals.

$$m_t = \left(\rho_0 - \frac{\int_0^L \int_0^{r_0} r R(r, t) Z(z, t) dr dz}{\int_0^L \int_0^{r_0} r dr dz} \right) V_s \quad (16)$$

Performing this integration then allows for calculation of the mass of gas loss from the sample and is presented in equation (17).

$$m_t = \left(\rho_0 - \frac{32(\rho_0 - \rho_i)}{\pi^2} \sum_{m=1}^{\infty} \frac{e^{-\lambda_m^2 r_0^2 \left(\frac{t}{\tau}\right) \left(\frac{1}{r_0}\right)}}{(\lambda_m r_0)^2} \sum_{n=0}^{\infty} \frac{e^{-(2n+1)^2 \pi^2 \left(\frac{t}{\tau}\right) \left(\frac{1}{L}\right)}}{(2n+1)^2} \right) V_s \quad (17)$$

While the sample is releasing gas to the container environment, the pressure in the container continues to rise until the sample pressure and container pressure reach an equilibrium which is given by equation (18), where P_i is the initial evacuation pressure, P_s is the initial sample charging pressure, V_c is the volume of the container, and P_f is the equilibrium pressure.

$$P_i V_c + P_s V_s \varepsilon = P_f (V_c + V_s \varepsilon) \quad (18)$$

Using these equations allows for the determination of the interconnected void fraction from (18). Then the molecular flow coefficient can be found by fitting (17) with the measured container pressure as a function of time and adjusting with D^k/ε . Figure 1 displays an example of this fitting with the pristine machined and cleaved tests. The closeness of fit supports the validity of the mathematical treatment outlined in equations (8) through (18). Lastly, D^k can be found by multiplying D^k/ε with the interconnected void fraction as determined from equation (18).

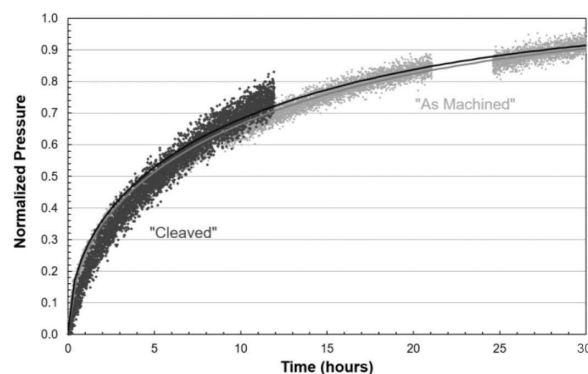


Figure 1. Measured data with fitted curve overlay of pristine cleaved and machined samples. Curves are calculated using equation (17) showing close agreement with experimental data.

Table 5. Results from the pristine samples using dynamic pycnometry.

	Machined	Cleaved
P_s (kPa)	748.29	727.74
P_f (kPa)	2.25	1.38
D^k/ϵ (cm ² /s)	6.0×10^{-7}	6.0×10^{-7}
D^k (cm ² /s)	1.2×10^{-8}	8.3×10^{-9}
ϵ	0.019	0.014

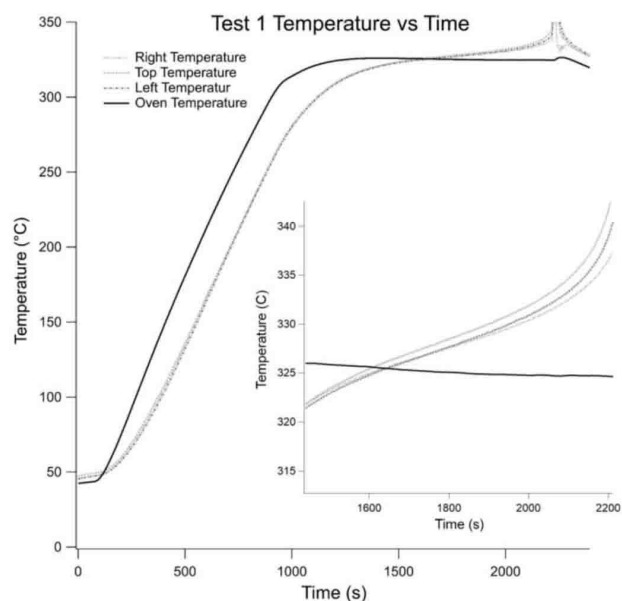
Table 5 displays the results for the pristine samples (Table 1), with one test per sample type being conducted. Thermally damaged samples (Table 2), machined in the axial and orthogonal directions (with respect to the original pressing axis) were tested in duplicate, and the results are presented in Table 6.

These results show that the machined orientation of the two samples had an insignificant effect on both flow parameters. Comparing the flow rates between the pristine and thermally damaged samples, it was found that the flow coefficient through the damaged samples were approximately 10^4 times greater than the flow through the pristine samples. Furthermore, the interconnected void fraction was found to increase by approximately 50% in the thermally damaged samples. However, flow in both sample types remains within the diffusive regime, with viscous flow remaining insignificant.

3.2 Gas-Generation Experiment

3.2.1 Temperature Data

Eight tests were conducted for the gas-generation experiment. Sample surface temperature was measured in three separate locations for each test (thermocouples visible in Figure 4). Figure 2 is the temperature data vs time for Test 1 and is representative for all of the gas-generation tests that were conducted. Self-heating is evident when the sample temperature exceeds the oven temperature. Cookoff occurs at the rapid temperature spike. These data were collected at 1 Hz and do not provide sufficient resolution to determine the peak temperature reached during this event.

**Figure 2.** Temperature data for Test 1 which is representative of all tests. Inset displays self-heating until cookoff.

Labels for surface locations (right, top, and left) are from the perspective of the high-speed video.

3.2.2 High-Speed Video

For all tests, high-speed video was shot at 4,000 fps, which was sufficient [13] to witness the deconsolidating deflagration behavior observed in all tests. During cookoff, no visible gas emission is observed prior to the mechanical failure of the sample, and once macro-cracking occurs, gas is emitted to the oven environment obscuring visual access to the sample. The first visible sign of reaction occurs 3 to 5 s prior to the peak of the dynamic pressure pulse. Figure 3 shows two frames taken from Test 3 with macro-cracking visible. The left frame was taken just prior to visible gas emission, and the right frame approximately 0.13 seconds after.

Table 6. Results from the thermally damaged samples using dynamic pycnometry.

	Axial Test 1	Test 2	Orthogonal Test 1	Test 2
P_s (kPa)	697.89	698.58	694.72	700.85
P_f (kPa)	9.10	9.10	9.58	9.72
D^k/ϵ (cm ² /s)	3.5×10^{-3}	3.0×10^{-3}	2.5×10^{-3}	4.5×10^{-3}
D^k (cm ² /s)	1.0×10^{-4}	8.6×10^{-5}	6.9×10^{-5}	1.3×10^{-4}
ϵ	0.030	0.029	0.028	0.029

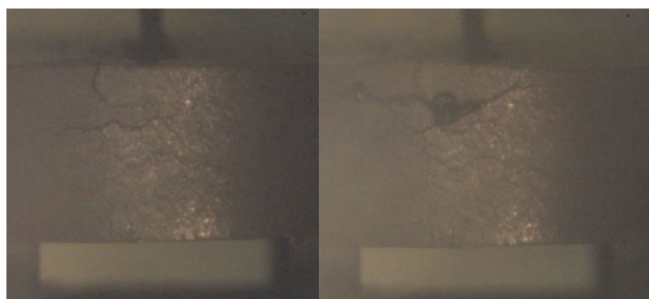


Figure 3. Two high-speed frames taken from Test 3 showing mechanical failure during deflagration.

3.2.3 Time-Lapse

Time-lapse images were recorded for all tests with a 10 second inter-frame period and provides a visible record of the evolving thermal damage. Three frames from Test 1 (Figure 4) show the evolution from a pristine yellow to ther-



Figure 4. Time-lapse of Test 1, which is representative of all tests. Thermocouples can be seen touching the surface of the sample.

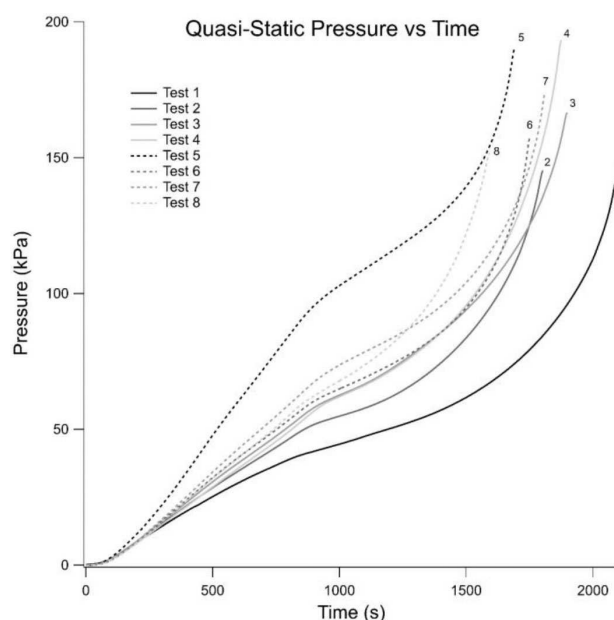


Figure 5. Quasi-static pressure for all eight tests conducted. Inflection points from ideal gas expansion to same off-gassing are found on each curve in the highlighted region.

mally damaged black over a duration of 2250 s. All eight tests exhibited similar color change.

3.2.4 Pressure Data

The quasi-static data for each test were recorded at a rate of 1 Hz, and are shown in Figure 5. Two separate regions of interest can be seen in all eight tests that were conducted. The first is the ideal gas expansion of pre-existing air in the oven which traces out an expected approximately linear path to the time at which the oven reaches its set point and the associated inflection point. Next, the sample starts to off-gas, and pressure in the oven rises until cookoff occurs. This last region provides the information relevant for the calculation of gas generated by the explosive.

Dynamic pressure data during cookoff were captured at 1 MHz for 20 seconds. Figure 6 displays these. The average peak pressure reached for all eight tests is 2.94 MPa with a standard deviation of 0.14 MPa. The repeatability of peak pressure between samples with nominally identical volume indicates that the entire mass of the sample is uniformly incorporated during the dynamic cookoff event.

The quasi-static data presented in Figure 5 and respective test temperature data was then used to determine how varying the surface area of each series affected the rate of gas-generation evolved prior to cookoff. The ideal gas law is differentiated with respect to time (keeping volume constant) to generate an expression for the molar gas generation rate (equation 19).

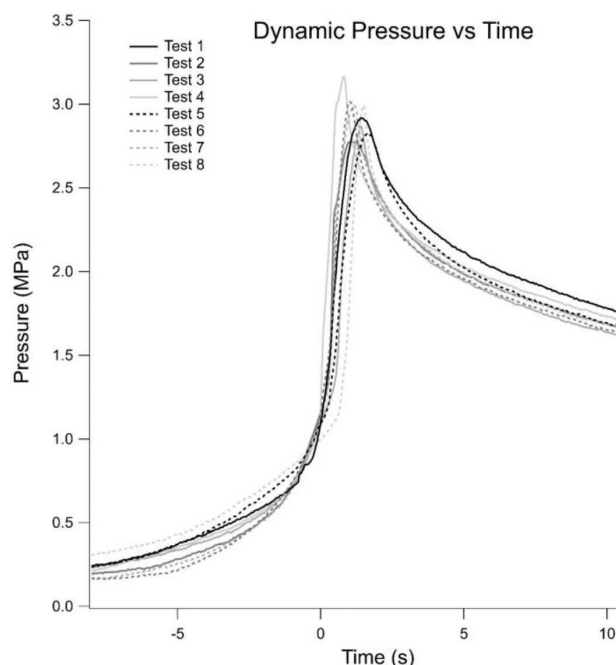


Figure 6. Dynamic pressure data for all eight tests showing high repeatability between tests.

$$\dot{n} = \frac{VP}{RT} \left(\frac{\dot{P}}{\bar{P}} - \frac{\dot{T}}{\bar{T}} \right) \quad (19)$$

A region of interest for quasi-static gas generation by the PBX 9502 was extracted starting with 0.08 $\mu\text{mol/s}$ and ending at 1 $\mu\text{mol/s}^2$. This region is chosen to ignore the initial spurious pressure rise from heating the ambient gas in the oven and to truncate the pressure rise before the dynamic cookoff event. These threshold values were varied to confirm that results were independent of boundary choice. Figure 7 displays the resulting gas-generation curves, within the region of interest, for each test using the defined threshold values.

Each curve was then averaged to produce a mean gas-generation rate for each test. Table 7 presents these values for the tests conducted.

Finally, these mean gas-generation rates were plotted against the sample surface area, Figure 8. A line of best fit was created to assess the linear relationship between gas-

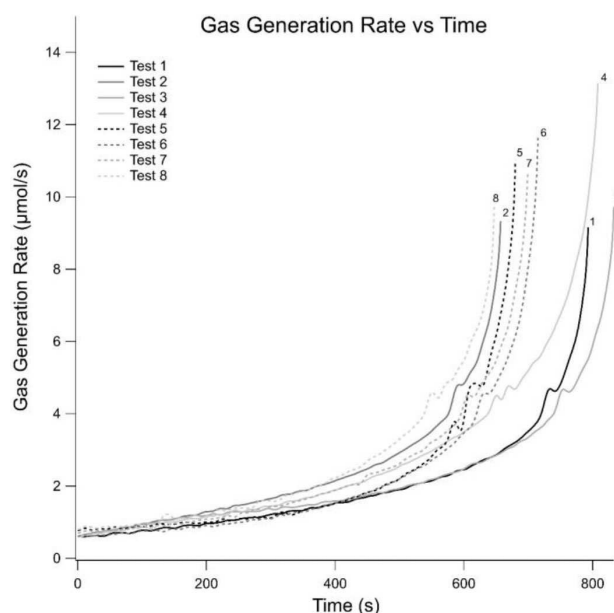


Figure 7. Gas generation rate vs time for all eight tests

Table 7. Mean gas-generation rate for each test.

Test Number	Test Series	Mean Gas-Generation Rate ($\mu\text{mol/s}$)	Surface Area (mm^2)
1	A	2.19	628 \pm 3
2	C	2.44	815 \pm 6
3	B	2.29	942 \pm 9
4	D	2.97	1170. \pm 8
5	A	2.11	628 \pm 3
6	C	2.49	815 \pm 6
7	B	2.46	942 \pm 9
8	D	2.71	1170. \pm 8

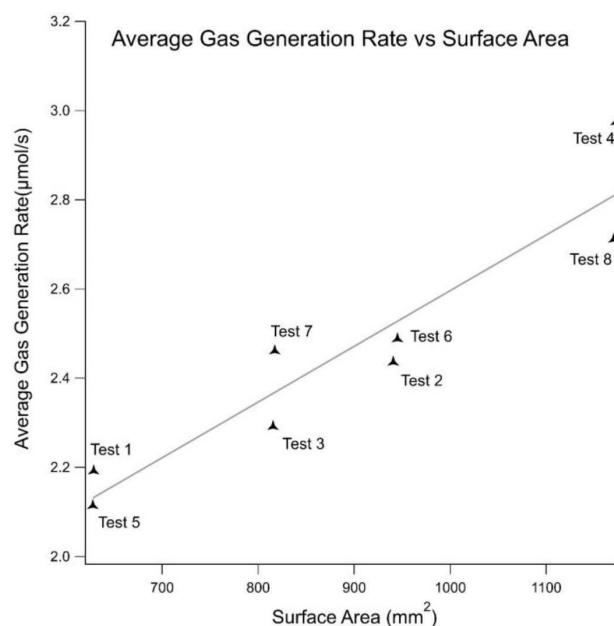


Figure 8. Average gas generation rate vs surface area with line of best fit.

generation rate and surface area. The coefficient of determination for this line was 0.89, indicating a significant linear dependency.

This analysis reveals that changing the surface area of these samples significantly alters the detectable molar rate of gas production. From this, it is inferred that gas generated interior to the sample remains trapped within the sample's total void volume until cookoff. The trapped gas builds pressure until it exceeds the mechanical strength of the material and failure occurs. The first visible indication of cookoff is the formation of large surface cracks. This macro-cracking serves to release internally trapped gas, and gas generation transitions from a surface-dominated regime to a volume-dominated regime. The entire sample becomes uniformly incorporated in the following deflagration, as each test series reached a reproducible final pressure state that is dependent on sample mass.

4 Conclusions

Two experiments were conducted to examine the gas transport behavior in PBX 9502 and analyze how this behavior thermally evolves. The first flow experiment utilized a gas permeameter and dynamic pycnometry to determine the molecular flow coefficient and interconnected void fraction for this composition. Two machined orientations were tested to examine how the anisotropic crystal structure of this material effects both parameters. Thermally damaged samples were tested against pristine ones, and the effects of surface machining smearing were investigated. The gas

permeameter was unable to resolve the molecular flow coefficient of the explosive, as it was found to be of the same order of magnitude as the PTFE seal used in this experiment. Dynamic pycnometry was used to determine both gas transport parameters. Values for the molecular flow coefficient were found to be approximately four orders of magnitude greater in the thermally damaged samples than in the pristine. However, even in these damaged samples, gas flow dynamics remained within the diffusive regime, with viscous Darcy flow playing an insignificant role. The effect of machining smearing was negligible. These findings show how the internal void structure in this composition effectively remains isolated from the external skin, limiting gaseous interaction to the diffuse regime.

Gas generation testing was then conducted to study the dynamic thermal evolution of gas transport via rate measurements. Four separate sample types had nominally identical masses with varying surface areas. Larger surface area samples were found to generate gas at faster rates than smaller surface area samples. Supporting the flow experiment results, these data show that detectible gas production from thermally evolving samples originates from the exterior skin. However, decomposition products are still produced inside the isolated internal void structure. Eventually, void pressure buildup exceeds the mechanical strength of the material, and macro-cracks relieve this stress. The previously trapped decomposition products then vent to the environment, which allows the entire sample to become uniformly incorporated in the following deflagration.

Acknowledgments

This work is supported by the United States Department of Energy through Los Alamos National Laboratory. Los Alamos National Laboratory is operated by Triad National Security, LLC, for the National Nuclear Security Administration (Contract No. 89233218CNA000001). We would like to thank John McAfee and Peter Dickson for providing insightful conversation and knowledge throughout the evolution of this research.

References

- [1] B. W. Asay, Cookoff, in *Shock Wave Science and Technology Reference Library*, Vol. 5, B. W. Asay, Ed., New York, Springer-Verlag Berlin Heidelberg, **2010**, pp. 403–482.
- [2] G. R. Parker, P. J. Rae, Mechanical and Thermal Damage, in *Shock Wave Science and Technology Reference Library*, Vol. 5, B. W. Asay, Ed., New York, Springer-Verlag Berlin Heidelberg, **2010**, pp. 293–393.
- [3] P. Dickson, G. R. J. Parker, P. J. Rae, *The Thermal Response of TATB-Based PBXs*, Los Alamos National Laboratory, LAUR: 1520327, Los Alamos, **2015**.
- [4] M. D. Holmes, G. R. Parker, P. Dickson, B. A. Meyer, C. C. Schmidt, Pressure Dependence of Slow Cookoff Behavior in PBX 9502 Bucket Tests, *15th Symposium (International) on Detonation*, San Francisco, CA, USA, July 13–18, **2014**.
- [5] A. Cuauhtemoc, G. Parker, M. Holmes, *Simulations of Two Heavily Confined PBX 9502 Cook-off Experiments*, Los Alamos National Laboratory, LAUR: 1821834, Los Alamos, **2018**.
- [6] R. McGuire, C. Tarver, Chemical-Decomposition Models for the Thermal Explosion of Confined HMX, TATB, RDX, and TNT Explosives, *7th Symposium (International) on Detonation*, Annapolis, MD, USA, June 16–19, **1981**.
- [7] M. L. Hobbs, M. J. Kaneshige, Ignition experiments and models of a plastic bonded explosive (PBX 9502), *J. Chem. Phys.* **2014**, *140*, no. 124203.
- [8] S. I. Jackson, Deflagration Phenomena in Energetic Materials: An Overview, in *Shock Wave Science and Technology Reference Library*, Vol. 5, New York, Springer-Verlag Heidelberg Berlin, **2010**, pp. 245–292.
- [9] F. Dullien, *Porus Media Fluid Transport and Pore Structure*, New York, Academic Press, INC., **1979**, pp. 75–85.
- [10] R. Schwarz, C. Liu, D. G. Thompson, *Anisotropy in the Ratchet Growth of PBX 9502*, Los Alamos National Laboratory, LAUR: 1521827, Los Alamos, **2015**.
- [11] R. B. Bird, W. E. Stewart, E. N. Lightfoot, *Transport Phenomena*, New York: John Wiley & Sons, **2007**.
- [12] H. Carslaw, J. Jaeger, *Conduction of Heat in Solids*, Oxford University Press, **1959**.
- [13] R. Fifer, J. Cole, Transitions From Laminar Burning For Porous Crystalline Explosives, *7th Symposium (International) on Detonation*, Annapolis, MD, USA, June 16–19, **1981**.

Manuscript received: September 25, 2019

Revised manuscript received: January 24, 2020

Version of record online: March 26, 2020